



Electronegative diversity induced localized built-in electric field in a single phased $\text{MoS}_x\text{Se}_y\text{N}_z$ for selectivity-enhanced visible photocatalytic CO_2 reduction

Deng Long^{a,1}, Jia Liu^{b,1}, Hongyu Chen^a, Pei Liu^a, Kai Zheng^{a,c}, Yibo Zeng^a, Xinyi Chen^{a,*}, Shuang Li^{b,*}, Miao Lu^{a,*}

^a Pen-Tung Sah Institute of Micro-Nano Science & Technology, Xiamen University, Xiamen 361005, PR China

^b School of Materials Science and Engineering, Nanjing University of Science and Technology, Nanjing 210094, PR China

^c School of Science, Jimei University, Xiamen 361021, PR China

ARTICLE INFO

Keywords:

Photocatalytic CO_2 reduction
Quarternary TMDs
Electronegativity
Selectivity
Built-in electric field

ABSTRACT

How to passivate the recombination in a photocatalyst is a big challenge to achieve efficient photocatalytic CO_2 reduction. Besides the heterojunction strategy, the design of intrinsic built-in electric field in a single phased photocatalyst can facilitate the transport while it does not introduce extra side reactions induced by the unbalanced photocarriers. This work utilizes the electronegative diversity between chalcogens and non-chalcogen element in a quarternary transition metal dichalcogenide of $\text{MoS}_x\text{Se}_y\text{N}_z$ to define localized built-in electric fields. It has been revealed that the nitrogen induced intrinsic dipole moments and potential energy have strengthened the built-in electric fields, promoting the separation of photocarriers and the gathering of electrons around N sites, which has been found to improve the adsorption of intermediate products and lower the energy for methanol-oriented photoproduction route. Finally, the $\text{MoS}_x\text{Se}_y\text{N}_z$ has improved the photoproduction of methanol reduced from CO_2 by 162%.

1. Introduction

The industrial development in the last decades has consumed a huge amount of fossil fuels, resulting in the emission of several billion tons of carbon dioxide that cause the intensive greenhouse effect and other environmental problems [1]. Thus, the capture and recycling of CO_2 has become an urgent demand for sustaining development [2]. Photocatalytic CO_2 reduction, combining the usage of solar energy and recycling of CO_2 to small organic fuel molecules, is widely considered as a promising solution to the above issue [3]. Since 1979, Inoue et al. [4] first reported photo-induced carbon dioxide reduction with TiO_2 . Tremendous works have been done to continuously explore new semiconductors for photocatalytic CO_2 reduction such as metal oxides (TiO_2 , WO_3 , ZnO , etc.) [5–8], metal sulfide of CdS [9], Ag- and Bi-based photocatalysts (Ag_3PO_4 , Bi_2MoO_6 , etc.) [10,11]. Generally, the photocatalytic CO_2 reduction has to overcome two main challenges to realize industrial application. One is to achieve highly efficient conversion in the visible windows [12]. The other is to achieve high selectivity in the

production, which requires a precise design on the photocarrier transport. The variety of valence states of carbon could involve up to eight electrons during the reduction of CO_2 , which is sensitively influenced by the energy level alignment on the active site of the photocatalyst. Thus, photocatalysts with a finely tunable band structure would be perfect for that purpose.

The semiconducting two-dimensional (2D) materials such as transition metal dichalcogenides (TMDs) have been regarded as a very promising photocatalyst for CO_2 reduction due to the visible absorption and continuously tunable band edge [13], while multivariate elements can further enlarge the tunable ranges of band structure [14]. For example, the ternary MoS_xSe_y had exhibited a tunable band gap between 1.64 eV and 1.82 eV [15]. Additionally, the atomic thickness of 2D materials has shortened the photocarrier diffusion distance and thus enhanced the carrier transport [16].

However, the TMDs still have to overcome some challenges before qualified for practical photocatalytic CO_2 reduction [12]. The strong intrinsic recombination in a single phased TMDs still inhibits the

* Corresponding authors.

E-mail addresses: chenxinyi@xmu.edu.cn (X. Chen), lishuang@njut.edu.cn (S. Li), lm@xmu.edu.cn (M. Lu).

¹ These authors contributed equally to this work.

effective electron transport for photocatalytic CO₂ reduction. A typical solution to intrinsic recombination is to employ the dual-excitation Z-type heterojunction to facilitate the separation of photocarriers [17]. Nevertheless, there is a side effect of heterojunction, which is that the different nature of materials on the two sides would result in unbalanced carriers in the interface. The unbalanced carriers would not transport along the Z-scheme path, which is possible to transfer directly to CO₂ to trigger a side reaction [18]. In a multivariate TMDs material, such as the ternary MoS_xSe_y, the electronegativity among the non-metallic elements could be slightly different i.e. 2.58 for that of S and 2.55 for that of Se, which might give a directional force to induce the carrier transport. However, the difference in electronegativity between S and Se is not big enough to form a strong built-in electric field to favor the separation of photocarriers [19,20]. When excited by light, due to the high scattering probability [21], the photogenerated electrons in the *d*-orbital of Mo atom have very close chance to transfer either to S or Se position, which cannot form a directed transport and thus the severe recombination still exists. Under this consideration, this work has introduced nitrogen as the third non-metallic element into the ternary MoS_xSe_y lattice to form the quaternary TMDs of MoS_xSe_yN_z. The electronegativity of N is 3.04, which is much higher than that of S or Se. Therefore, the dipole of N-S and N-Se is more polarized than that of S-Se, which might induce the gathering of electrons around the N sites i.e. the separation of photocarriers might be favored. Thus, the built-in electric field formed via the photogenerated electron-hole pairs would be strengthened, which would be probably favor a directed carrier transport of the photocarriers inside the material and inhibit the recombination. The enhanced built-in electric field has also promoted the gathering of electrons around N sites, which has been found to improve the adsorption of intermediate products and lower the energy for methanol-oriented photoproduction route. The built-in electric field featured MoS_xSe_yN_z as a single phased photocatalyst has improved the photoproduction of methanol by 162% compared to MoS_xSe_y. Meanwhile, the quantum selectivity of methanol production has been also increased by 13% accordingly.

2. Experimental section

2.1. Chemicals

Molybdenum trioxide (MoO₃, Aladdin, 99.5%), selenium powder (Se, Aladdin, 99.99%), sulfur powder (S, Sinopharm Chemical Reagent Co., Ltd (China), > 99.0%), NaHCO₃, (Xilong Chemical Co. Ltd (China), > 99.5%).

3. Synthesis of photocatalysts

3.1. MoS_xSe_y synthesis

The MoS_xSe_y was synthesized on the surface of quartz glass via Chemical Vapor Deposition (CVD) method in a tube furnace with double temperature zones. Sulfur and selenium powders used as the source of S and Se were placed in the up-stream zone with the temperature of 200 °C. The MoO₃ powder was placed in the down-stream zone with the temperature of 750 °C, while the quartz glass sheets were placed downstream. A mixed gas flow of 100 sccm H₂ and 400 sccm Ar was introduced as the reacting and carrying-protecting gas respectively. The deposition was set to 1 h while the pressure was kept at 200 Pa.

3.2. MoS_xSe_yN_z synthesis

Under the normal pressure, the synthesized quartz glass MoS_xSe_y material was placed at the central zone of the tube furnace under the temperature of 750 °C with the heating rate of 5 °C per minute, where the mixed gas flow of 30 sccm NH₃ and 200sccm Ar was introduced as the reacting and carrying-protecting gas, respectively. The temperature was kept for one hour and the furnace was cooled down to room

temperature naturally.

4. Characterization

The morphology and structure were characterized by via scanning electron microscopy (SEM, Carl Zeiss Supra 55), high-resolution transmission electron microscopy (HRTEM, JEOL2100), X-ray diffraction (XRD, Rigaku Ultima IV) and X-ray Photoelectron Spectroscopy (XPS, Quantum 2000). The optical properties were studied using UV-Vis absorption spectrometer (Shimadzu UV-2600), photoluminescence (PL, Hitachi F-7000) and Raman spectrometer (excited by 532 nm diode-pumped solid-state laser). The photoelectrochemical measurements including Mott-Schottky measurement, photocurrent and electrochemical impedance spectra (EIS) were conducted by electrochemical workstation equipped with three electrode system (Shanghai Chenhua Instrument Co., LTD CHI660E). Atomic force microscopy (AFM, Cypher S, Asylum) equipped with Ti/Ir coated silicon tip (Asytec 01-R2) was employed to trace the surface smoothness (tapping mode) as well as the corresponding potential distribution (scanning Kelvin probe microscopy).

5. Photoelectrochemical measurements

The Quartz glass-MoS_xSe_y and MoS_xSe_yN_z electrodes were characterized in a three-electrode configuration using a Ag/AgCl reference electrode (in 3 M KCl aqueous solution) and a platinum sheet counter electrode. 0.1 M Na₂SO₄ aqueous solution was used as electrode solution (pH 6.21). The potential of the working electrode was read from its current open-circuit voltage. The Mott-Schottky measurement was carried out with different frequency of 500 Hz and 1000 Hz, the calibration of potentials was referred to the reversible hydrogen electrode (RHE) according to Eq. (1) [22].

$$E(\text{vs-RHE}) = E(\text{vs Ag/AgCl}) + 0.197 \text{ V} + 0.0591 \times \text{pH} \quad (1)$$

And the photoelectrode was irradiated with a solar simulator (AM 1.5 G, 300 W) to do the photocurrent measurement with 100 s interval on-off for total 1100 s

6. Photocatalytic CO₂ reduction

The photocatalytic CO₂ reduction was carried out under 0.2 Mpa CO₂ in a sealed autoclave at room temperature, and 0.1 M NaHCO₃ was used as the hydrogen source. An AM 1.5 G calibrated solar simulator (Sirius 300 P, 320–780 nm, 300 W, Zolix) equipped with a 420 nm longpass filter ($\lambda \geq 420 \text{ nm}$) was used as the light source. Gas chromatography (GC 9790) equipped with both gas and liquid analysis columns under flame ionization detector was used to detect gas phase and liquid phase products, respectively.

7. Results and discussion

The highly dense 2D MoS_xSe_y and MoS_xSe_yN_z nanosheets are found vertically stand and uniformly distributed on a 5 cm sized substrate, with the size around 2–4 μm (Fig. 1a, d, S1 and S2), demonstrating the controllability and stability of the as-proposed synthesis which is suitable for mass production. The increased conductivity of the insulating substrate after growth of nanosheets (Fig. S2), has further proved the high density and uniformity of the nanosheets. HRTEM images shown in Figs. 1b and 1c have revealed that as-prepared MoS_xSe_y and MoS_xSe_yN_z nanosheets have the hexagonal lattice structure (2 H phase), while the stacking of (002) facets with the distance of ~0.637 nm can be identified (Fig. S3). Also, the (100) facets with *d*-spacing of ~0.275 nm can be observed. And the 2D structure of MoS_xSe_y nanosheets is from double-layered to multi-layered (Fig. S4), while 2–4 layers might be the main structure (Fig. S5). The inset of Fig. 1d and Fig. S5 verify the ultrathin 2D

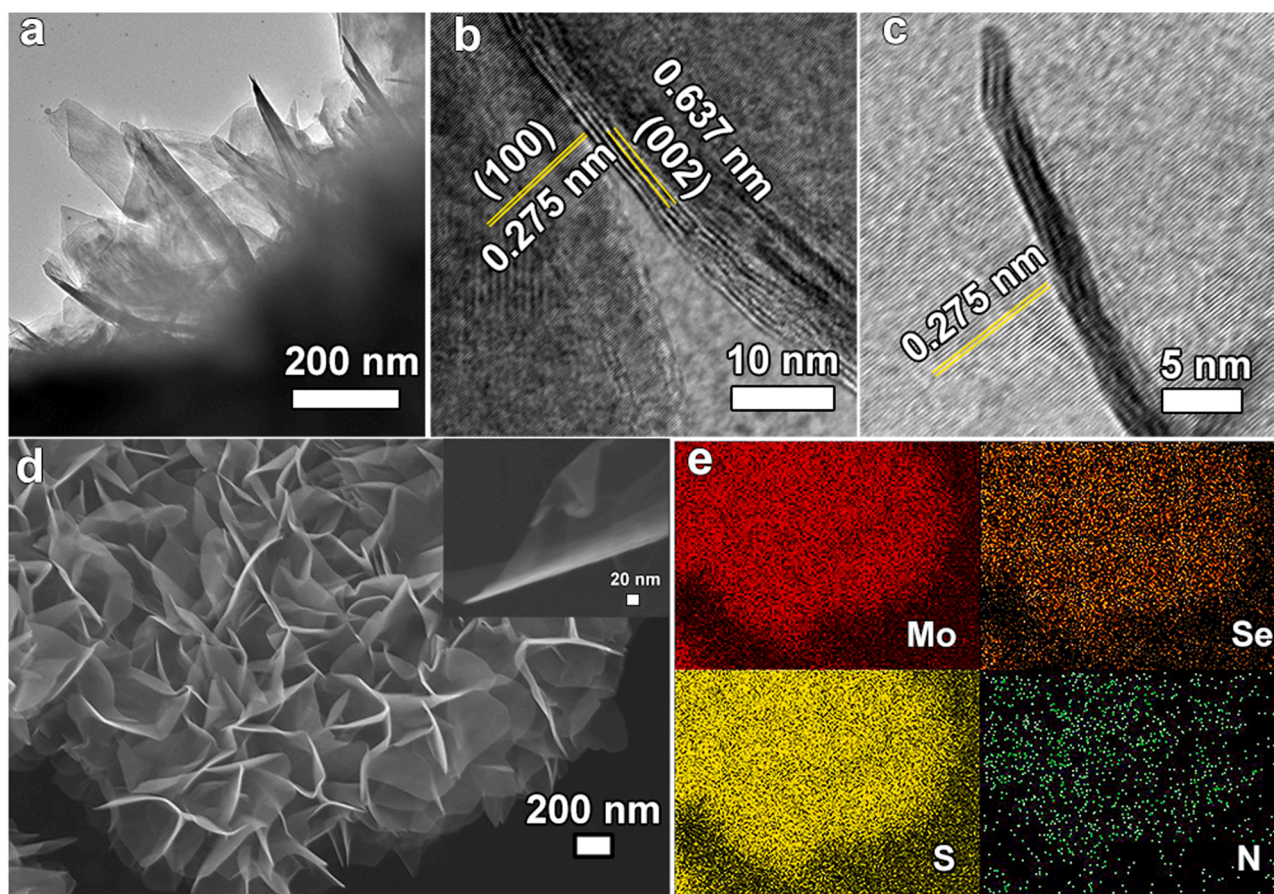


Fig. 1. (a) TEM and (b) HRTEM images of MoS_xSe_y nanosheets; (c) HRTEM and (d) SEM images of $\text{MoS}_x\text{Se}_y\text{N}_z$ nanosheets; and (e) EDX elemental mapping of Mo (red), Se (brown), S (yellow) and N (green) in $\text{MoS}_x\text{Se}_y\text{N}_z$.

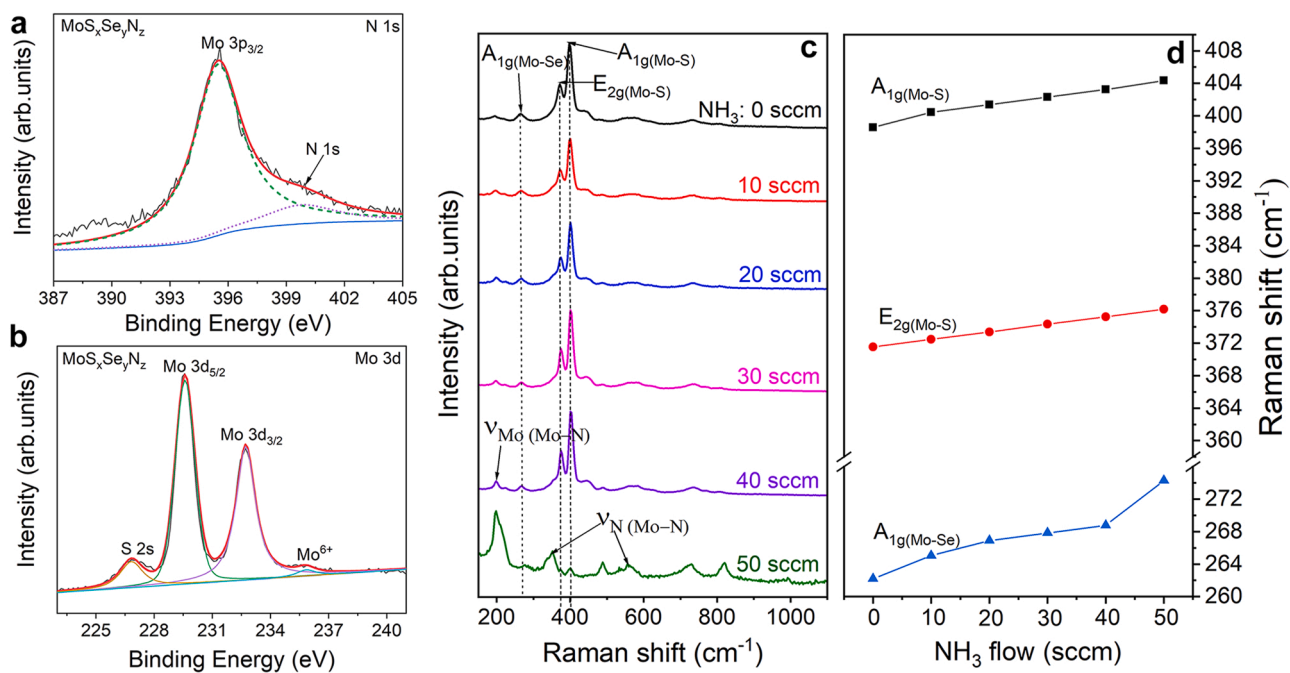


Fig. 2. XPS of $\text{MoS}_x\text{Se}_y\text{N}_z$ at (a) Mo 3d and (b) Mo 3p, N 1s; (c) Raman spectra from MoS_xSe_y to $\text{MoS}_x\text{Se}_y\text{N}_z$ excited under 532 nm laser and (d) shift of Mo-S [$E_{2g}(\text{Mo-S})$, $A_{1g}(\text{Mo-S})$] and Mo-Se related modes [$A_{1g}(\text{Mo-Se})$] with varying NH_3 flow rates.

structure of MoS_xSe_y nanosheets. Although the electronegativity of N is much higher than that of S or Se, the $\text{MoS}_x\text{Se}_y\text{N}_z$ had maintained the original structure of MoS_xSe_y , indicating the introduction of N atoms and the corresponding bonding did not obviously change the lattice structure or form new phases. The energy dispersive X-ray (EDX) spectra shown in Table S1 has verified the presence of nitrogen in the structure of $\text{MoS}_x\text{Se}_y\text{N}_z$, while the elemental mapping for Mo, S, Se, and N shows that nitrogen had been uniformly and discretely added to the MoS_xSe_y nanosheets, as shown in Figs. 1d and 1e. By comparing the elements of MoS_xSe_y and $\text{MoS}_x\text{Se}_y\text{N}_z$, it can be concluded from Table S1 that the content of Se had been lowered with the presence of N.

The presence of nitrogen has been further traced by XPS and Raman spectra as shown in Fig. 2, S6 and S7. The Mo 3d signals in XPS (Fig. 2a) at ~ 229.6 and 232.7 eV corresponding to Mo 3d_{5/2} and Mo 3d_{3/2} could be observed in both MoS_xSe_y and $\text{MoS}_x\text{Se}_y\text{N}_z$, while $\text{MoS}_x\text{Se}_y\text{N}_z$ exhibited another small peak at ~ 235.9 eV that was attributed to the existence of Mo^{6+} [23,24]. Accordingly, the signal at ~ 399.9 eV near the ~ 395.5 eV of Mo 3p_{3/2}, corresponding to N 1s (Fig. 2b) could be also identified only in $\text{MoS}_x\text{Se}_y\text{N}_z$. The signal of Mo^{6+} and N 1s implies the Mo-N bonding in $\text{MoS}_x\text{Se}_y\text{N}_z$. On the other hand, the position of nitrogen in the lattice has been further studied by tracing the Raman shifts of $\text{MoS}_x\text{Se}_y\text{N}_z$ with continuously varying NH_3 flow rates (from 0 to 50 sccm) used in the fabrication. As shown in Figs. 2c and 2d, the typical modes [15,25] of Mo-S [$A_{1g}(\text{Mo-S})$, $E_{2g}(\text{Mo-S})$] are found to be fading out gradually with the increase of nitrogen. Similarly, the Mo-Se [$A_{1g}(\text{Mo-Se})$] mode [15,25] has also exhibited the same trend. The mode at 197.8 cm^{-1} might be attributed to the Mo vibration of Mo-N bonding and the corresponding N vibration is observed at 354.9 cm^{-1} and 557.2 cm^{-1} [26–28], while the intensity of those are found to be strengthened with continuous increase of NH_3 flow rates. It should be also noticed that the Mo-S and Mo-Se related modes blue-shifted with

the increase of nitrogen, as shown in Fig. 2d. The $A_{1g}(\text{Mo-S})$ mode shifted from 398.6 cm^{-1} to 404.3 cm^{-1} , and the $E_{2g}(\text{Mo-S})$ shifted from 371.5 cm^{-1} to 376.6 cm^{-1} . More obviously, the mode of $A_{1g}(\text{Mo-Se})$ shifted from 262.2 cm^{-1} to 274.3 cm^{-1} . As mentioned above, the HRTEM and XRD results suggest that the hexagonal structure has been maintained in $\text{MoS}_x\text{Se}_y\text{N}_z$ i.e. there was no new phase forming during the introduction of nitrogen. It can be deduced that nitrogen has been successfully inserted into the lattice of MoS_xSe_y and probably settled down in the non-metal positions.

The MoS_xSe_y has exhibited two TMDs based typical absorption peaks at 615 nm and 675 nm, respectively, while those of the $\text{MoS}_x\text{Se}_y\text{N}_z$ have shifted to 610 nm and 670 nm, as shown in Fig. 3a. Correspondingly, the band gap of MoS_xSe_y and $\text{MoS}_x\text{Se}_y\text{N}_z$ extracted from absorption spectra based on Tauc's relation is 1.50 eV and 1.60 eV, respectively (Fig. S8a), indicating that the additional nitrogen might slightly broaden the band gap because of the strong electronegativity of nitrogen in Mo-N bonding. The broadening of band gap from MoS_xSe_y to $\text{MoS}_x\text{Se}_y\text{N}_z$ can be further verified by $E_g = E_{\text{CBM}} - E_{\text{VBM}}$, while E_{CBM} is the conduction band minimum (CBM) measured by Mott-Schottky method [29], and E_{VBM} is the valence band maximum (VBM) extracted from valence band XPS (Fig. S8). It shows that the CBM is -1.34 eV (-0.73 eV vs. RHE) for MoS_xSe_y , and -1.42 eV (-0.81 eV vs. RHE) for $\text{MoS}_x\text{Se}_y\text{N}_z$. Meanwhile, the VBM is 0.75 eV for MoS_xSe_y , and 0.80 eV for $\text{MoS}_x\text{Se}_y\text{N}_z$. Therefore, the band gap deduced from CBM and VBM would be 1.48 eV and 1.61 eV , respectively, in consistence with the Tauc's relation derived band gaps. To further investigate the evolution of electronic structure from a ternary MoS_xSe_y to the quaternary $\text{MoS}_x\text{Se}_y\text{N}_z$, density Functional Theory (DFT) calculation was employed to analyze the band structure of MoS_xSe_y ($x, y = 0-2$) with part of non-metal positions replaced by N atoms, as shown in Fig. S9. The Vienna Ab Initio Simulation Package (VASP) with the projector-augmented wave (PAW)

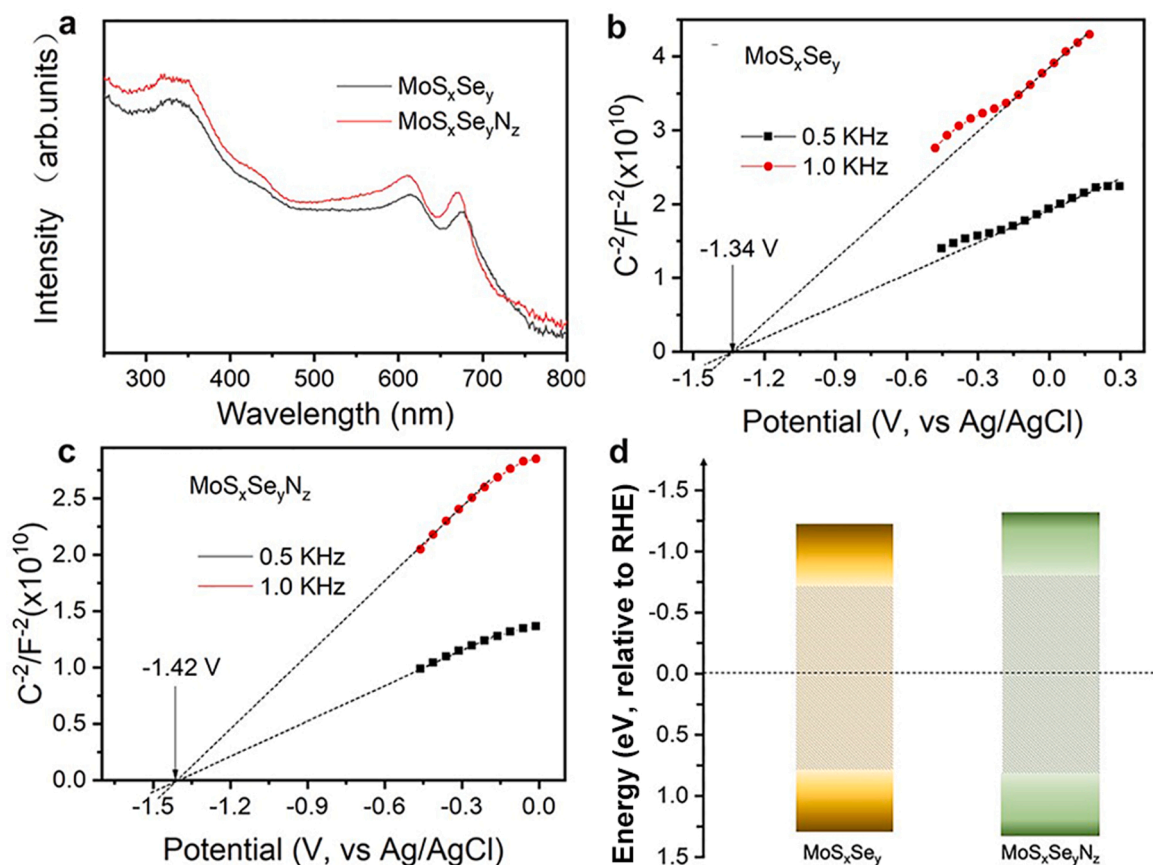


Fig. 3. (a) UV-vis absorption spectra of MoS_xSe_y and $\text{MoS}_x\text{Se}_y\text{N}_z$; (b) Mott-Schottky plots of MoS_xSe_y and (c) $\text{MoS}_x\text{Se}_y\text{N}_z$; (d) band gap extracted from UV-vis absorption spectra based on Tauc's relation, and checked via CBM extracted from (b), (c) and VBM extracted from valence band XPS in Fig. S8.

method was used for all DFT calculations[30,31]. The generalized gradient approximation (GGA) with Perdew-Burke-Ernzerhof (PBE) algorithm[32] was selected to describe the exchange-correlation functional. The long-range van der Waals force has been considered in calculations by DFT-D3 approach[33]. The vacuum layers are larger than 15 Å in structure models to restrain the interaction between adjacent layers. The Monkhorst-Pack k-mesh grid was sampled with $9 \times 9 \times 1$ for unit cell calculations. The energy cut-off, convergence criteria for the electronic and ionic relaxation steps are 400 eV, 1×10^{-4} eV/cell and 0.05 eV/Å, respectively to ensure the calculation accuracy. The results show that in the case of two-layered TMDs MoS_2 and MoSe_2 , the band gap has been found enlarged with presence of 1.39% N (Fig. S10). Consequently, according to the evolution of band structure from MoS_xSe_y to $\text{MoS}_x\text{Se}_y\text{N}_z$ as shown in Fig. 3d, it should be noticed that with the band gap broadening of $\text{MoS}_x\text{Se}_y\text{N}_z$, the CBM has been also raised up a bit, from which an enhanced reduction potential can be predicted reasonably.

Furthermore, the DFT calculation carried in different S/Se ratio of MoS_xSe_y structure (Fig. S9) also shows that with a proper percentage of N in the lattice, the band gap of $\text{MoS}_x\text{Se}_y\text{N}_z$ will be slightly enlarged and the CBM will be lowered a bit (Fig. S10). More importantly, the DFT calculation has predicted that due to the difference in electronegativity of S, Se and N, the nitrogen induced dipole moment and potential energy will be greater. Once part of chalcogens replaced by N atoms in MoS_xSe_y , known as $\text{MoS}_x\text{Se}_y\text{N}_z$, the nitrogen induced intrinsic dipoles of N-S and N-Se will be much stronger than that of S-Se, hopefully to facilitate the separation of photocarriers. By comparing the intrinsic dipoles in Janus-structured MoSSe , MoSN and MoSeN using DFT, it is found that the dipole moment in different sites change with the pairs based on different

elements, i.e. of N-Se ($0.061 \text{ e}\cdot\text{\AA}$) > N-S ($0.040 \text{ e}\cdot\text{\AA}$) > S-Se ($0.036 \text{ e}\cdot\text{\AA}$), as shown in Fig. S11. Correspondingly, the evolution of potential energy has been also found increased from MoSSe to MoSN and MoSeN . Furthermore, the DFT calculation for a uniform $\text{MoS}_x\text{Se}_y\text{N}_z$ shown in Fig. 4a has also revealed that the dipole induced difference in the potential energy ΔV has been enhanced at N-Se pair (1.28 eV) with the dipole moment pointing from Se to N (Fig. 4b). Based on the non-uniform potential distribution in $\text{MoS}_x\text{Se}_y\text{N}_z$ as shown in Fig. 4c, the potential ΔV in N-Se pair is theoretically predicted to be the highest. Correspondingly, the nitrogen induced potential difference could be also traced via the AFM working in Kelvin probe microscopy mode [34], as shown in Fig. 5. MoS_xSe_y had exhibited an indistinguishable potential distribution. On the opposite, the potential distribution of $\text{MoS}_x\text{Se}_y\text{N}_z$ had obviously shown a non-uniform trace. Since the Kelvin probe microscopy was taken in a constant-distance mode, the potential distribution should be uniform as long as the dipole moments along the material was uniform regardless of the surface roughness, which is the case of MoS_xSe_y . Once there is a discretely distributed element with obviously different electronegativity, such as nitrogen, the dipole moments at those regions will be different and then result in a non-uniform potential distribution as the theoretical analysis suggested. The non-uniform potential distribution implies localized gathering of electrons, which is most likely to occur around the N sites as described in Fig. 4d, could be favorable for the CO_2 adsorption and production of high value added products reduced from CO_2 .

In addition, the photoluminescence (PL) of $\text{MoS}_x\text{Se}_y\text{N}_z$ was quenched compared to that of MoS_xSe_y , while the luminescence lifetime [35] had been prolonged from 2.90 ns to 4.05 ns, as shown in Fig. 6a and b, implying that the intrinsic recombination of photocarriers was not that

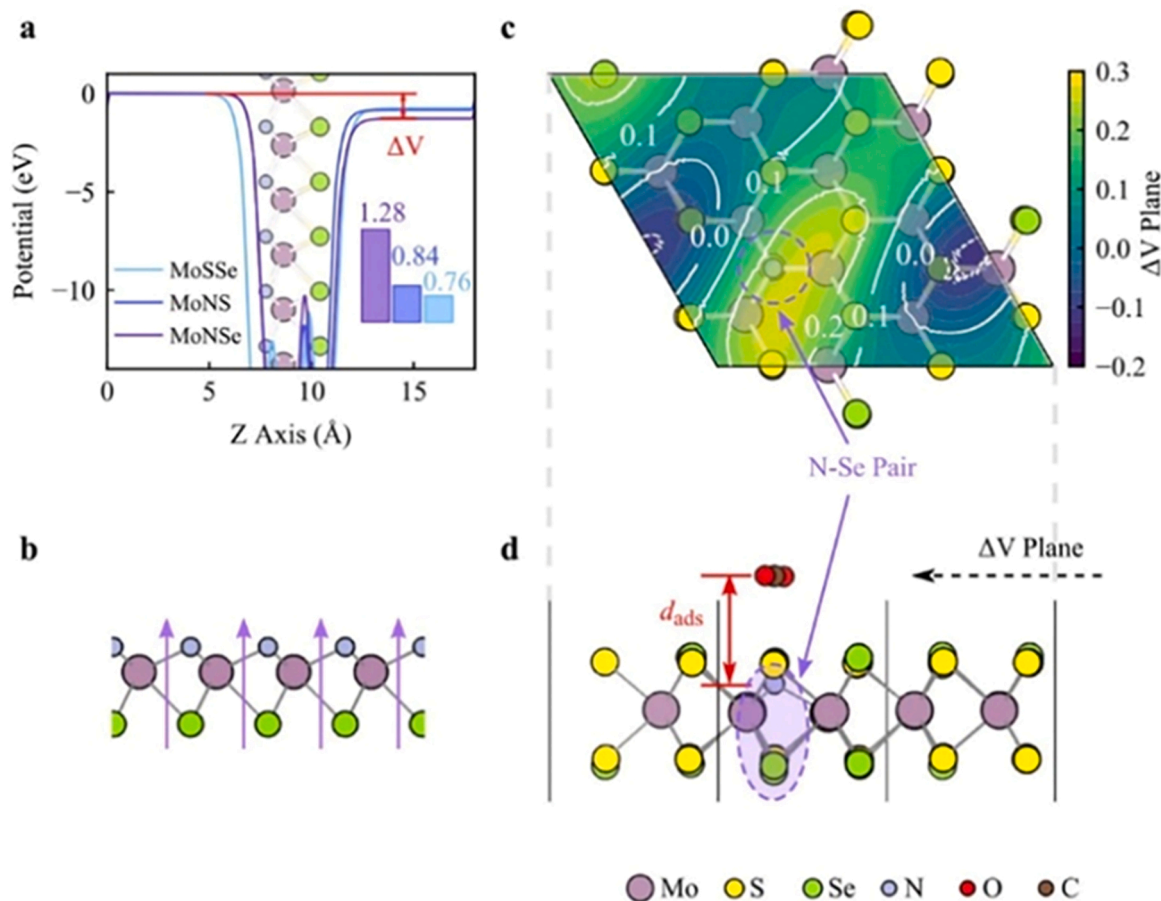


Fig. 4. DFT calculation of (a) potential energy difference (ΔV) among bondings based on different atoms; (b) dipole moment formed in the N-Se pair structure; (c) distribution of potential energy difference (ΔV) in $\text{MoS}_x\text{Se}_y\text{N}_z$ structure projected along z-axis and (d) adsorption of CO_2 at N site of $\text{MoS}_x\text{Se}_y\text{N}_z$ structure.

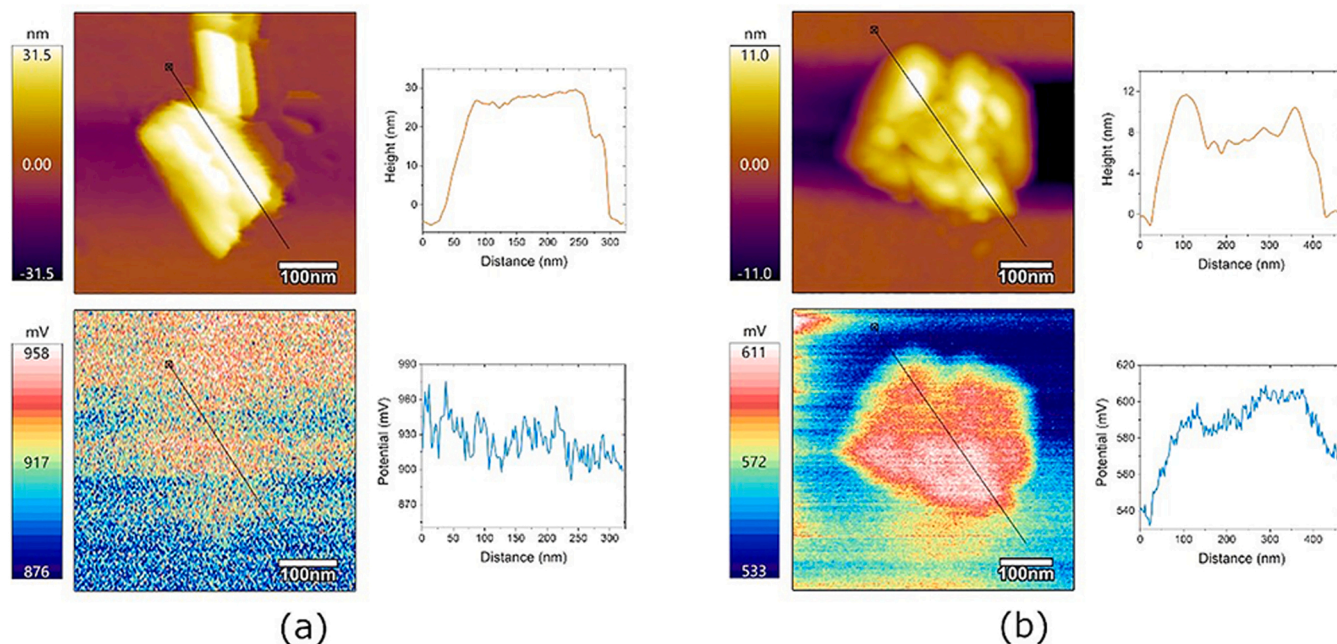


Fig. 5. Height (upper) and potential (lower) traces in AFM of (a) MoS_xSe_y and (b) $\text{MoS}_x\text{Se}_y\text{N}_z$. The linear change in height and potential along the labelled line starting from the square mark are shown in the spectrum type as well.

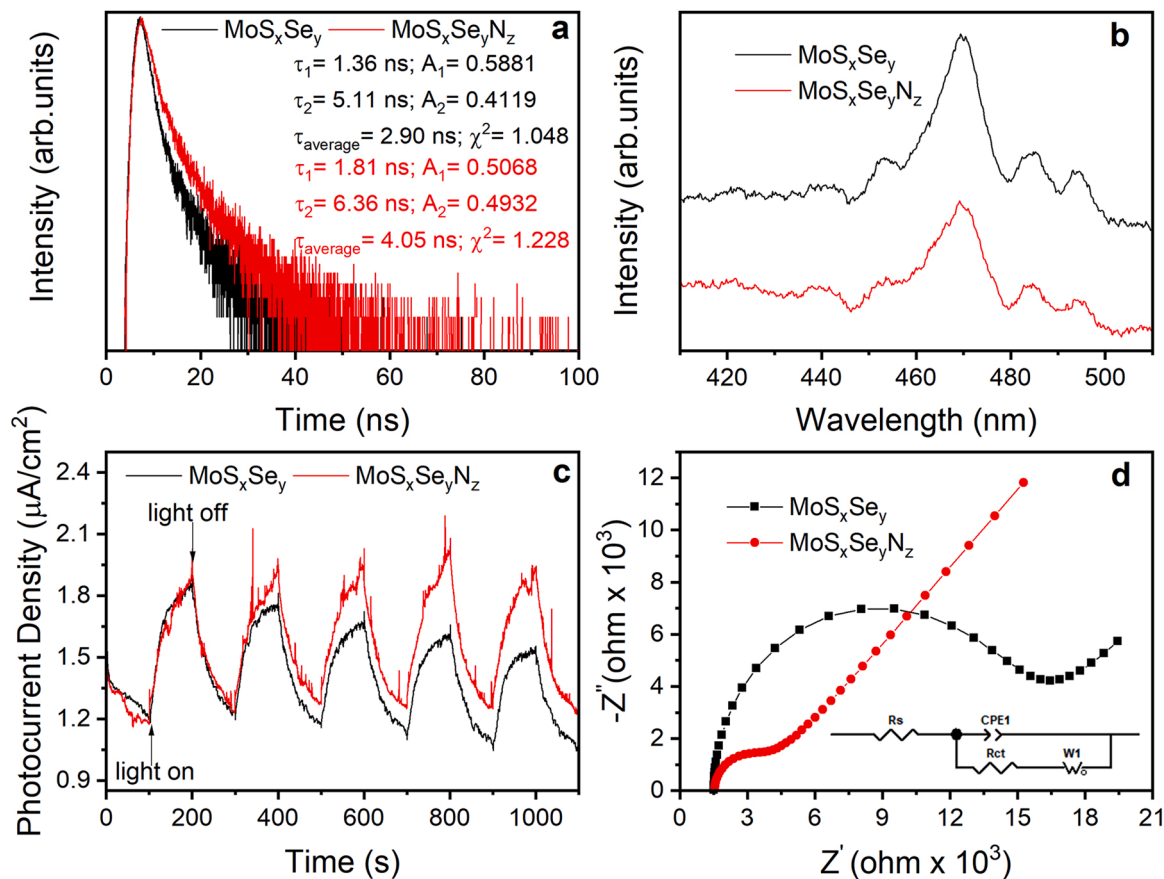


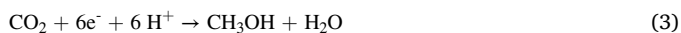
Fig. 6. (a) Time-resolved PL; (b) PL spectra; (c) photocurrent responses and (d) EIS of MoS_xSe_y and $\text{MoS}_x\text{Se}_y\text{N}_z$.

significant in $\text{MoS}_x\text{Se}_y\text{N}_z$ compared to MoS_xSe_y , and the photocarrier transport in $\text{MoS}_x\text{Se}_y\text{N}_z$ could be profited from that. The enlarged difference in electronegativity has made the intrinsic dipole moments between N and chalcogens i.e. N-S and N-Se dipole much stronger than that

formed among chalcogens (S-Se), which means the bonding electrons are closer to N atoms. Also, with the presence of Mo-N bonding, the N atoms would be in the form of N^{3-} , which means each N atom needs one more electron than S or Se to form stable bonding with Mo. In that case,

there would be more holes around the N sites to maintain the electric neutrality. Therefore, the discrete enhanced built-in electric fields pointing from N regions to non-N regions could form, inducing a directed photocarrier transport to favor the separation of photocarriers. The enhanced photocarrier transport and built-in electric field might also lead to an increased photocurrent [36]. As shown in Fig. 6c, the average on/off photocurrent density of MoS_xSe_yN_z is about 0.7 $\mu\text{A}/\text{cm}^2$, which is a bit larger than that of 0.51 $\mu\text{A}/\text{cm}^2$ in MoS_xSe_y. Meanwhile, EIS was also employed to study the surface/interface reaction kinetics and the nature of resistances, as shown in Fig. 6d. [37–39]. The Nyquist plot of MoS_xSe_yN_z has exhibited a smaller semicircle than that of MoS_xSe_y, from which the charge-transfer resistance (R_{ct}) of MoS_xSe_yN_z and MoS_xSe_y were extracted to be 3.8 K Ω and 15.6 K Ω , respectively. The relatively smaller R_{ct} on the surface of MoS_xSe_yN_z might also imply a favored photocarrier transport, which might be corresponding to the enhanced built-in electronic field induced N-S and N-Se dipoles, facilitating a directed photocarrier transport. Generally, with a higher CBM i. e. enhanced reducing capability and facilitated photocarrier transport, MoS_xSe_yN_z could be predicted to perform better on photocatalytic CO₂ reduction.

Fig. 7 and S12 show the performance of MoS_xSe_y and MoS_xSe_yN_z on photocatalytic CO₂ reduction. The presence of a carbon-fixed product of CH₃OH could be observed, with two additional gases i.e. CO and CH₄ had been also detected. Both MoS_xSe_y and MoS_xSe_yN_z have revealed a long-term stability of photocatalytic CO₂ reduction under visible irradiation, while MoS_xSe_yN_z obtained in 30 sccm NH₃ has the best performance among MoS_xSe_yN_z. The electrons for CO₂ reduction to different carbon products showing as the following formulas [40]:



It is clear that 6 electrons are needed for the generation of each CH₃OH molecule (Eq. (3)), while only 2 electrons are required by CO production (Eq. (2)) and 8 for CH₄ (Eq. (4)). For MoS_xSe_y, the production rate of CH₃OH is 1.79 $\mu\text{mol g}^{-1}\text{h}^{-1}$, while the production rates of CO and

CH₄ are 3.21 $\mu\text{mol g}^{-1}\text{h}^{-1}$ and 0.27 $\mu\text{mol g}^{-1}\text{h}^{-1}$, respectively. Quantum selectivity for CH₃OH production calculated via (Eqn. S1) is 56%. For MoS_xSe_yN_z, the production rate of CH₃OH has been improved by ~162% to 4.69 $\mu\text{mol g}^{-1}\text{h}^{-1}$, nearly three times over that of MoS_xSe_y. The production of CO has been obviously weakened, and production of CH₄ has been increased a bit to 1.31 $\mu\text{mol g}^{-1}\text{h}^{-1}$. Quantum selectivity for CH₃OH production in MoS_xSe_yN_z has been increased to 69%. The production rate of CH₃OH has been increased by about three times and the corresponding selectivity has been increased by 13% with the presence of nitrogen. The optimized production rate and quantum selectivity for CH₃OH in the single phased MoS_xSe_yN_z has demonstrated the positive effect on the photocatalytic performance, with the presence of non-metallic elements beyond the chalcogens i.e. nitrogen. The presence of nitrogen in MoS_xSe_yN_z induced intrinsic dipoles of N-S and N-Se have been found stronger than that of S-Se, which could enhance the localized built-in electric fields pointing from N regions to non-N regions i.e. photogenerated electrons would be more likely to move toward and gather around N sites. Thus, the high concentration of photogenerated electrons around the N sites has made them very active for the reduction of CO₂, where the electrons might preferably transfer to CO₂ trigger the production of high value added products. On the opposite site, the excited holes also gathered beyond N sites under the enhanced built-in electric field to complete the oxidation courses. In a word, the built-in electric field enhanced by strong electronegativity of nitrogen has favored the separation and transport of photocarriers to improve the photocatalytic performance. Meanwhile, it should be noticed that the production rates of both CH₃OH and CH₄ in MoS_xSe_yN_z has been improved, while that of CO was weakened. Since production of CO requires only 2 electrons, which is the most straightforward production of reducing CO₂, the decrease of CO production rate would also imply that the presence of nitrogen in the lattice might be also favorable for the capture of CO₂ and intermediate product [41], inducing further electron transferring and the forming of complicated products.

To elucidate the specific role of nitrogen in the electron transport for photocatalytic CH₃OH production in details, the adsorption of intermediate products around different elements among the surface of MoS_xSe_yN_z had been further studied via DFT calculation. At the

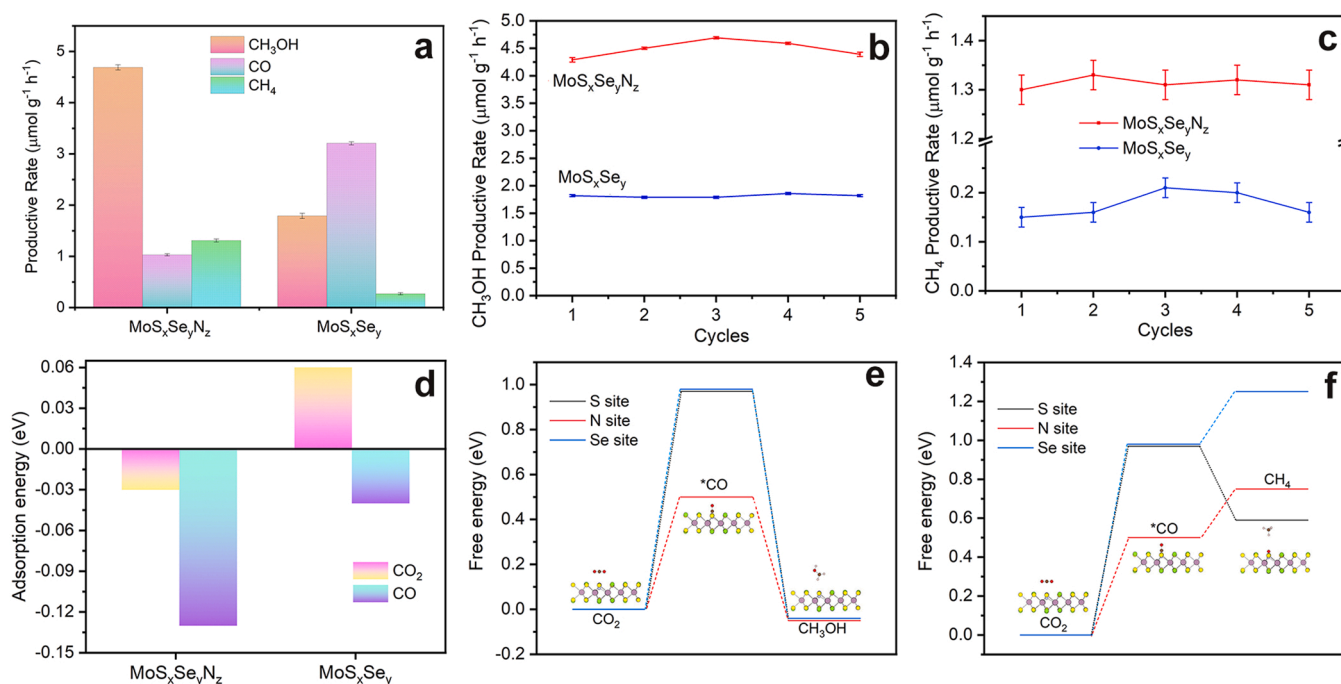


Fig. 7. (a) The Photocatalytic CO₂ reduction productivity of MoS_xSe_y and MoS_xSe_yN_z; stability of (b) CH₃OH production and (c) CH₄ production; (d) DFT calculation of adsorption energy of CO₂ and CO; (e) free energy of CH₃OH route and (f) CH₄ route at S, N and Se sites.

beginning of a complete photocatalytic CO₂ reduction process, photocarriers are generated and separated while the catalyst excited by light, and CO₂ molecules are adsorbed on the surface of the catalyst [40]. It has been found in Fig. 7d that the adsorption energy ΔE_{ad} of CO₂ on the N sites is negative i.e. exothermic rather than positive i.e. endothermic on the chalcogen sites, indicating a more stable adsorption of CO₂ on the N sites. Once the electrons transfer to CO₂, CO₂ begins to be reduced through two potential routes that are competing with each other: fast hydrogenation (FH) and fast deoxidization (FdO, known as the carbene mechanism) [42]. Since CH₃OH and CH₄ were both observed in the products, the as-proposed MoS_xSe_y and MoS_xSe_yN_z would be more likely to follow a carbene-dominant route. Firstly, the adsorbed CO₂ is reduced to *COOH and then reduced to *CO, as shown in Fig. S13 (CH₃OH route) and S14 (CH₄ route) [43]. The calculated free energy has revealed this step needs much less energy at N sites than that at either S or Se sites, indicating that the CO₂ reduction will be more likely to start at N site. The DFT calculation has also shown a more stable adsorption of CO at the N sites (Fig. 7d), which is favorable for the following reaction. On the other hand, the relatively weaker absorption of CO on MoS_xSe_y surface might cause the desorption of CO and thus lower the chance of the following reaction. Besides, the DFT calculation has also predicted that the further reaction for converting *CO to the next intermediate products would be also more straightforward to occur at N sites rather than S or Se sites due to the advantage of low energy need for the reaction at N sites, in both CH₃OH route (Fig. S13) and CH₄ route (Fig. S14). Therefore, CO is the main product on the MoS_xSe_y, while MoS_xSe_yN_z would have a higher chance to conduct the following reactions, which has been verified by the obviously weakened photocatalytic CO production of MoS_xSe_yN_z compared to MoS_xSe_y. Meanwhile, as mentioned before, the dipole of N-Se and N-S would result in the gathering of electrons around N site to trigger multi-electrons involved production like CH₄ and CH₃OH. Since the electrons required for CH₃OH production (6 electrons) are a few less than that for CH₄ production (8 electrons), the production of CH₃OH might be more straightforward. Accordingly, Fig. 7e and S13 have shown that around N site the CH₃OH route could occur spontaneously due to the decrease on energy from *CO to CH₃OH. However, for the CH₄ route, more extra energy and electrons are needed for the following reaction (Fig. 7f and S14). It has been also shown (Fig. S15) that the adsorption energy of CH₃OH is low, indicating a higher chance for the desorption of CH₃OH to stop the potential following reaction.

Therefore, the production rate of CH₃OH has been found to be obviously higher than that of CH₄ on both MoS_xSe_y and MoS_xSe_yN_z. Generally, at the essential step of CO₂ to *CO, which requires extra energy, the N-Se dipole enhanced built-in electric field has provided abundant electrons on the surface of MoS_xSe_yN_z that also has a stronger adsorption of *CO to conduct the following reactions. As a result, the productivity and selectivity of CH₃OH have been enhanced in MoS_xSe_yN_z compared to MoS_xSe_y.

The original mechanism in the band structure of the enhancement of photocatalytic performance from MoS_xSe_y to MoS_xSe_yN_z is discussed. As commonly known, the strong recombination of photocarriers in a single phased photocatalyst hinders the gathering of photogenerated electrons and their transport from photocatalyst to CO₂, resulting in a relatively low production rate. The intrinsic built-in electric field is not strong enough to realize efficient separation of photocarriers. The weak gathering of photogenerated electrons cannot provide CO₂ sufficient electrons for a multi-step reduction to obtain high value added products, which makes the photocatalytic product from a single phased photocatalyst is usually dominated by CO that only induces two electrons, as shown in Table S2. The ternary elemental design of MoS_xSe_y actualizes the precise band alignment for selective production of photocatalytic CO₂ reduction, yet the difference in electronegativity between S and Se is not significant enough to hinder recombination and form strong built-in electric field, providing sufficient electrons to facilitate a multi-step photoreduction of CO₂. In that case, CO is still the main product from

MoS_xSe_y. On the contrary, a quarternary MoS_xSe_yN_z with the presence of a non-chalcogen element, nitrogen, would have a different band structure. The strong electronegativity of nitrogen helps to form strong built-in electric fields and gather the photogenerated electrons around, has demonstrated a CH₃OH dominant production in the photocatalytic CO₂ reduction. It should be noticed that according to the EDX results the content of nitrogen in MoS_xSe_yN_z was just a little, and the photocurrent of MoS_xSe_yN_z was just a bit higher than that of MoS_xSe_y as well. However, the production rate of CH₃OH of MoS_xSe_yN_z has been significantly increased, indicating that the improvement should not be mainly attributed to an increased photocarrier concentration, but was due to a more effective and directed transport, as well as a more straightforward CH₃OH oriented reaction route, with the presence of nitrogen. It can be concluded that the electronegative diversity between chalcogens and nitrogen induced strong dipole moments has effectively facilitated the gathering and transport of photogenerated electrons to trigger the high value added production.

8. Conclusion

MoS_xSe_yN_z nanosheets has been synthesized for photocatalytic CO₂ reduction. The difference in electronegativity among the non-metal elements has been used to form strong dipoles to favor the separation of photocarriers and thus enhance the built-in electric field. Therefore, the gathering of photogenerated electrons around N sites has improved the multi-electron involved photoreduction from CO₂ to CH₃OH by 162%.

CRediT authorship contribution statement

Deng Long: Conceptualization, Methodology, Validation, Formal analysis, Investigation, Writing – original draft, Visualization. **Jia Liu:** Software, Formal analysis. **Hongyu Chen:** Validation, Formal analysis. **Pei Liu:** Formal analysis. **Kai Zheng:** Formal analysis. **Yibo Zeng:** Formal analysis. **Xinyi Chen:** Conceptualization, Methodology, Investigation, Resources, Writing – review & editing. Supervision, Project administration, Funding acquisition. **Shuang Li:** Software, Formal analysis, Resources. **Miao Lu:** Resources, Supervision, Funding acquisition.

Declaration of Competing Interest

The authors declare that they have no known competing financial interests or personal relationships that could have appeared to influence the work reported in this paper.

Data Availability

Data will be made available on request.

Acknowledgement

This work was supported by Fujian Provincial Department of Science and Technology of China (No. 2021H0010), and the Natural Science Foundation of China (No. 62174142). We thank Ms. Lingling Zheng for the technical support on electron microscopy.

Appendix A. Supporting information

Supplementary data associated with this article can be found in the online version at [doi:10.1016/j.apcatb.2023.122625](https://doi.org/10.1016/j.apcatb.2023.122625).

References

- [1] S. Singh, A. Modak, K.K. Pant, A. Sinhamahapatra, P. Biswas, MoS₂-nanosheets-based catalysts for photocatalytic CO₂ reduction: a review, *ACS Appl. Nano Mater.* 4 (2021) 8644–8667.

- [2] J.M. Kolle, M. Fayaz, A. Sayari, Understanding the effect of water on CO₂ adsorption, *Chem. Rev.* 121 (2021) 7280–7345.
- [3] X. Sun, S. Jiang, H. Huang, H. Li, B. Jia, T. Ma, Solar energy catalysis, *Angew. Chem. Int. Ed.* 61 (2022), e2022048.
- [4] T. Inoue, A. Fujishima, S. Konishi, K. Honda, Photoelectrocatalytic reduction of carbon dioxide in aqueous suspensions of semiconductor powders, *Nature* 277 (1979) 637–638.
- [5] D. Long, J. Peng, H. Liu, Z. Feng, L. Chen, X. Chen, M. Lu, Graphene oxide discarded solution for high surface area photocatalyst, *Sol. Energy Mater. Sol. Cells* 209 (2020), 110446.
- [6] X. Chen, L. Liu, P.Y. Yu, S.S. Mao, Increasing Solar Absorption for Photocatalysis with Black Hydrogenated Titanium Dioxide Nanocrystals, *Science* 331 (2011) 746–750.
- [7] X. Chen, Jinhua Ye, Shuxin Ouyang, Tetsuya Kako, Zhaosheng Li, Z. Zou, Enhanced incident photon-to-electron conversion efficiency of tungsten trioxide photoanodes based on 3D-photon crystal design, *ACS Nano* 5 (2011) 4310–4318.
- [8] A. McLaren, Teresa Valdes-Solis, G. Li, S.C. Tsang, Shape and size effects of ZnO nanocrystals on photocatalytic activity, *J. Am. Chem. Soc.* 131 (2009) 12540–12541.
- [9] R. Zeng, K. Lian, B. Su, L. Lu, J. Lin, D. Tang, S. Lin, X. Wang, Versatile synthesis of hollow metal sulfides via reverse cation exchange reactions for photocatalytic CO₂ reduction, *Angew. Chem. Int. Ed. Engl.* 60 (2021) 2–10.
- [10] X. Yang, S. Wang, N. Yang, W. Zhou, P. Wang, K. Jiang, S. Li, H. Song, X. Ding, H. Chen, J. Ye, Oxygen vacancies induced special CO₂ adsorption modes on Bi₂MoO₆ for highly selective conversion to CH₄, *Appl. Catal. B* 259 (2019), 118088.
- [11] S.S. Tafreshi, A.Z. Moshfegh, N.H. de Leeuw, Mechanism of photocatalytic reduction of CO₂ by Ag₃PO₄(111)/g-C₃N₄ nanocomposite: a first-principles study, *J. Phys. Chem. C* 123 (2019) 22191–22201.
- [12] X. Jiao, K. Zheng, L. Liang, X. Li, Y. Sun, Y. Xie, Fundamentals and challenges of ultrathin 2D photocatalysts in boosting CO₂ photoreduction, *Chem. Soc. Rev.* 49 (2020) 6592–6604.
- [13] X. Sun, H. Huang, Q. Zhao, T. Ma, L. Wang, Thin-layered photocatalysts, *Adv. Funct. Mater.* 30 (2020) 1910005.
- [14] D. Long, J. Liu, L. Bai, L. Yan, H. Liu, Z. Feng, L. Zheng, X. Chen, S. Li, M. Lu, Continuously selective photocatalytic CO₂ fixation via controllable S/Se ratio in a TiO₂–MoS₂Se_y dual-excitation heterostructured nanotree, *ACS Photonics* 7 (2020) 3394–3400.
- [15] H. Li, Q. Zhang, X. Duan, X. Wu, X. Fan, X. Zhu, X. Zhuang, W. Hu, H. Zhou, A. Pan, X. Duan, Lateral growth of composition graded atomic layer MoS₂(1–x)Se₂(x) nanosheets, *J. Am. Chem. Soc.* 137 (2015) 5284–5287.
- [16] Z. Wei, B. Li, C. Xia, Y. Cui, J. He, J.-B. Xia, J. Li, Various structures of 2D transition-metal dichalcogenides and their applications, *small*, *Methods* 2 (2018) 1800094.
- [17] T. Su, Z. Qin, H. Ji, Z. Wu, An overview of photocatalysis facilitated by 2D heterojunctions, *Nanotechnol* 30 (2019), 502002.
- [18] Q. Xu, L. Zhang, B. Cheng, J. Fan, J. Yu, S-scheme heterojunction photocatalyst, *Chem* 6 (2020) 1543–1559.
- [19] M.S. Yoo, H.C. Lee, C. Wolf, N.N. Nguyen, D.-H. Park, J. Kim, E. Lee, H.-J. Chung, K. Cho, Growth of multilayer graphene with a built-in vertical electric field, *Chem. Mater.* 32 (2020) 5142–5152.
- [20] A.C. Riis-Jensen, M. Pandey, K.S. Thygesen, Efficient charge separation in 2D janus van der waals structures with built-in electric fields and intrinsic p–n doping, *J. Phys. Chem. C* 122 (2018) 24520–24526.
- [21] J. Xie, S. Li, X. Zhang, J. Zhang, R. Wang, H. Zhang, B. Pan, Y. Xie, Atomically-thin molybdenum nitride nanosheets with exposed active surface sites for efficient hydrogen evolution, *Chem. Sci.* 5 (2014) 4615–4620.
- [22] J. Xu, X. Li, W. Liu, Y. Sun, Z. Ju, T. Yao, C. Wang, H. Ju, J. Zhu, S. Wei, Y. Xie, Carbon dioxide electroreduction into syngas boosted by a partially delocalized charge in molybdenum sulfide selenide alloy monolayers, *Angew. Chem. Int. Ed. Engl.* 56 (2017) 9121–9125.
- [23] L. Wang, J. Shang, G. Yang, Y. Ma, L. Kou, D. Liu, H. Yin, D. Hegh, J. Razal, W. Lei, 2D higher-metal nitride nanosheets for solar steam generation, *Small* 18 (2022), e2201770.
- [24] D. Kiriya, P. Lobaccaro, H.Y. Nyein, P. Taheri, M. Hettick, H. Shiraki, C.M. Sutter-Fella, P. Zhao, W. Gao, R. Maboudian, J.W. Ager, A. Javey, General thermal texturization process of MoS₂ for efficient electrocatalytic hydrogen evolution reaction, *Nano Lett.* 16 (2016) 4047–4053.
- [25] H. Li, X. Duan, X. Wu, X. Zhuang, H. Zhou, Q. Zhang, X. Zhu, W. Hu, P. Ren, P. Guo, L. Ma, X. Fan, X. Wang, J. Xu, A. Pan, X. Duan, Growth of alloy MoS₂(_{2x})Se₂(_{1–x}) nanosheets with fully tunable chemical compositions and optical properties, *J. Am. Chem. Soc.* 136 (2014) 3756–3759.
- [26] F. Lin, H. Qin, T. Wang, L. Yang, X. Cao, L. Jiao, Few-layered MoN–MnO heterostructures with interfacial-O synergistic active centers boosting electrocatalytic hydrogen evolution, *J. Mater. Chem. A* 9 (2021) 8325–8331.
- [27] J. Xiong, W. Cai, W. Shi, X. Zhang, J. Li, Z. Yang, L. Feng, H. Cheng, Salt-templated synthesis of defect-rich MoN nanosheets for boosted hydrogen evolution reaction, *J. Mater. Chem. A* 5 (2017) 24193–24198.
- [28] E. Soignard, O. Shebanova, P.F. McMillan, Compressibility measurements and phonon spectra of hexagonal transition-metal nitrides at high pressure: ϵ -Ta₂N, δ -MoN, and Cr₂N, *Phys. Rev. B* 75 (2007), 014014.
- [29] S. Ravishanker, J. Bisquert, T. Kirchartz, Interpretation of Mott–Schottky plots of photoanodes for water splitting, *Chem. Sci.* 13 (2022) 4828–4837.
- [30] G. Kresse, J.F. Iler, Efficient iterative schemes for ab initio total-energy calculations using a plane-wave basis set, *Phys. Rev. B* 54 (1996) 169–185.
- [31] G. Kresse, J. Furthmüller, Efficiency of ab-initio total energy calculations for metals and semiconductors using a plane-wave basis set, *Comput. Mater. Sci.* 6 (1996) 15–50.
- [32] John P. Perdew, Kieron Burke, M. Ernzerhof, Generalized gradient approximation made simple, *Phys. Rev. Lett.* 77 (1996) 3865–3868.
- [33] S. Grimme, J. Antony, S. Ehrlich, H. Krieg, A consistent and accurate ab initio parametrization of density functional dispersion correction (DFT-D) for the 94 elements H–Pu, *J. Chem. Phys.* 132 (2010), 154104.
- [34] H. Ben, Y. Liu, X. Liu, X. Liu, C. Ling, C. Liang, L. Zhang, Diffusion-Controlled Z-scheme-steered charge separation across PDI/BiOI heterointerface for ultraviolet, visible, and infrared light-driven photocatalysis, *Adv. Funct. Mater.* 31 (2021) 2102315.
- [35] S. Wang, B.Y. Guan, X. Wang, X.W.D. Lou, Formation of hierarchical Co₉S₈@ZnIn₂S₄ heterostructured cages as an efficient photocatalyst for hydrogen evolution, *J. Am. Chem. Soc.* 140 (2018) 15145–15148.
- [36] X. Ma, M. Mai, H. Lin, L. Zeng, J. Zhang, H. Zhou, D. Chen, A novel electrochemical method for simultaneous measurement of real-time potentials and photocurrent of various photoelectrochemical systems, *J. Power Sources* 415 (2019) 99–104.
- [37] D. Vikraman, S. Hussain, K. Karupppasamy, A. Feroze, A. Kathalingam, A. Sanmugam, S.H. Chun, J. Jung, H.S. Kim, Engineering the novel MoSe₂–Mo₂C hybrid nanoarray electrodes for energy storage and water splitting applications, *Appl. Catal. B* 264 (2020), 118531.
- [38] M. Mojaddami, A. Simchi, Robust water splitting on staggered gap heterojunctions based on WO₃/WS₂–MoS₂ nanostructures, *Renew. Energy* 162 (2020) 504–512.
- [39] F. Ciucci, Modeling electrochemical impedance spectroscopy, *Curr. Opin. Electrochem.* 13 (2019) 132–139.
- [40] E. Gong, S. Ali, C.B. Hiragond, H.S. Kim, N.S. Powar, D. Kim, H. Kim, S.-I. In, Solar fuels: research and development strategies to accelerate photocatalytic CO₂ conversion into hydrocarbon fuels, *Energy Environ. Sci.* 15 (2022) 880–937.
- [41] J. Fu, K. Jiang, X. Qiu, J. Yu, M. Liu, Product selectivity of photocatalytic CO₂ reduction reactions, *Mater. Today* 32 (2020) 222–243.
- [42] T. Kong, Y. Jiang, Y. Xiong, Photocatalytic CO₂ conversion: what can we learn from conventional CO_x hydrogenation? *Chem. Soc. Rev.* 49 (2020) 6579–6591.
- [43] X. Jiao, X. Li, X. Jin, Y. Sun, J. Xu, L. Liang, H. Ju, J. Zhu, Y. Pan, W. Yan, Y. Lin, Y. Xie, Partially oxidized SnS₂ atomic layers achieving efficient visible-light-driven CO₂ reduction, *J. Am. Chem. Soc.* 139 (2017) 18044–18051.